JOURNAL OF AIRCRAFT
Vol. 41, No. 1, January–February 2004

New Roughness Computation Method and Geometric Accretion Model for Airfoil Icing

Guy Fortin*
Université du Québec à Chicoutimi, Chicoutimi, Quebec G7H 2B1, Canada
Adrian Ilinca†
Université du Québec à Rimouski, Rimouski, Quebec G5L 3A1, Canada
Jean-Louis Laforte‡
Université du Québec à Chicoutimi, Chicoutimi, Quebec G7H 2B1, Canada
and
Vincenzo Brandi§
Italian Aerospace Research Center, 81043 Capua, Italy

Recent developments are presented in wet and dry ice accretion simulation at the Anti-Icing Materials International Laboratory in a joint project with the Italian Aerospace Research Center. An analytical model is introduced to calculate the surface roughness and the remaining, runback, and shedding liquid water mass on an airfoil surface. Three analytical formulations are used to calculate the local roughness height based on the maximum height that a bead can reach before moving and the wave height on a water film. A mass balance is used to determine the remaining and runback water masses when the water state and the maximum bead height are known. The water shedding mass is determined using a simple mass model. A new method is used to build the accreted ice surface on the airfoils. It uses the bisection of the angle between adjacent panels to determine ice shape. The new roughness computation method and the geometric model generate the complex ice shapes observed experimentally, and the results agree well with icing profiles obtained in wind-tunnel experiments.

Nomenclature

A_b	=	frontal bead cross section, m^2
A_p	=	control volume surface, m^2
A_i	=	ice section, m^2
C_{cal}	=	calibration parameter
C_D	=	drag coefficient
C_f	=	friction coefficient
C_G	=	flow coefficient
d_d	=	median volumetric diameter, m
e_b	=	bead height before moving, m
e_f	=	film height, m
$e_{f\min}$	=	minimum film height, m
e_r	=	rivulet height, m
F_D	=	drag force, N
F_g	=	gravity force parallel to the surface, N
F_{grav}	=	gravity force, N
F_W	=	aerodynamic force, N
F_σ	=	rigidity force, N
f	=	solid fraction
f_{bw}	=	bead liquid fraction
g	=	gravitational acceleration, m/s^2
mb	=	slope
m_{cap}	=	impingement water mass, kg
m_{evap}	=	evaporative water mass, kg
m_{rbin}	=	incoming runback water mass, kg
m_{rbout}	=	outgoing runback water mass, kg
m_{resw}	=	residual mass, kg
m_{rmw}	=	remaining mass, kg
m_{shw}	=	shedding mass, kg
m_w	=	liquid water mass, kg
m_{wadm}	=	admissible liquid water mass, kg
R_g	=	gravitational flow ratio
R_w	=	aerodynamic flow ratio
r_b	=	bead radius, m
s	=	curvilinear abscissa, m
T_f	=	water solidification temperature, K
T_s	=	surface temperature, K
T_0	=	static temperature, K
U_e	=	airspeed at the edge boundary, m/s
U_w	=	wind speed at the bead level, m/s
U_∞	=	airspeed, m/s
V_b	=	bead volume, m^3
Δb	=	control volume width, m
Δt	=	time step, s
$\Delta\theta_c$	=	hysteresis contact angle, deg
θ_a	=	maximum contact angle, deg
θ_c	=	contact angle, deg
θ_r	=	minimum contact angle, deg
κ	=	local roughness, m
κ_s	=	equivalent sand-grain roughness, m
κ_0	=	initial object roughness, m
μ_a	=	air dynamic viscosity, Pa · s
μ_w	=	water dynamic viscosity, Pa · s
ρ_a	=	air density, kg/m^3
ρ_b	=	bead density, kg/m^3
ρ_i	=	ice density, kg/m^3
ρ_w	=	water density, kg/m^3
σ_w	=	water surface tension, N/m

Received 6 November 2002; presented as Paper 2003-1076 at the AIAA Aerospace Sciences Meeting and Exhibit, Reno, Nevada, 6–9 January 2003; revision received 28 February 2003; accepted for publication 6 March 2003.

*Graduate Student, Applied Sciences Department, 555 boulevard de l'Universite; guy_fortin@uqac.ca. Student Member AIAA.

†Professor, Engineering Department, 300, allee des Ursulines, Box 3300; adrian_ilinca@uqar.qc.ca.

‡Professor, Applied Sciences Department and Director of the Anti-Icing Materials International Laboratory, 555 boulevard de l'Universite; jean-louis_laforte@uqac.ca.

§Research Engineer, Applied Aerodynamic Laboratory, Centro Italiano Ricerche Aerospaziali, Maiorise; v.brandi@cira.it.

τ_w = wall shear stress, Pa
φ = surface inclination, deg

Introduction

DURING ice accretion processes, roughness develops on ice-covered surfaces. The roughness controls the boundary-layer development, which affects the convective heat transfer and the droplet collection efficiency, which in turn influence the ice shape. Although the importance of this factor is well recognized, not much has been done to investigate the surface roughness associated with ice accretion. The lack of information has been circumvented in numerical simulations by using empirical correlations for calculating the height of surface roughness or convective heat transfer coefficients. These correlations are developed by comparing computed ice shapes with a set of experimental results and selecting the surface roughness height or convective heat transfer coefficient that provides the best agreement with experimentation. This was developed in the empirical correlation reported by Shin and Bond,[1] which is currently used in most numerical models simulating airfoil ice accretions. This approach is helpful, but does not take into consideration the ice accretion physics and the actual condition of ice-covered airfoil surfaces. Indeed, the Shin and Bond[1] correlation, which is based on the definition of equivalent sand grain roughness,[2] is not truly representative of the size and distribution of the local surface height elements, especially when they are covered by water.[3] Therefore, numerical simulations based on physical roughness parameters will contribute to improve ice shape prediction on airfoils, especially in the wet growth regime.

Because no numerical simulation of airfoil icing involving calculated roughness height was found, an analytical model based on physical parameters was developed, in which the roughness surface elements are represented as beads, as defined in the Hansman and Turnock[4] study, and as a wave in the form of a film, as described by Al-Khalil et al.[5,6]

The iterative process involved in existing airfoil icing simulations contributes to render the surface continuous and smooth, which further averages heights of roughness elements. To counter and minimize this effect, a new method based on the bisection of the angle between adjacent panels is introduced, to add the mass of accreted ice as it grows.

The objective of this paper is to present a new analytical model for the calculation of roughness heights and a new geometric ice addition model, based on bisection of the angle between adjacent panels. The influence of these improvements on the simulation is studied by comparing mass and shape of ice accretion with experimental and previously reported results on the same airfoil.

Ice Accretion Model

The recognized general methodology used for the simulation of ice accretion on airfoils is based on the successive computation of airflow, water droplet trajectories, collection efficiency, heat transfer balance, and accreted ice. For this paper, the ice shapes are predicted using the two-dimensional CIRAMIL code, which comprises the aerodynamic algorithm developed by the Italian Aerospace Research Center (CIRA),[7] including potential flow, droplet trajectories, and collection efficiency, as well as a thermodynamic model developed by the Anti-Icing Materials International Laboratory (AMIL). This model, which is based on the equation derived by Messinger,[8] is similar to those reported by Wright,[9] Gent,[10] Guffond et al.,[11] Paraschivoiu,[12] and Minigione and Brandi.[7] The heat balance on each panel is the sum of the following energies: latent heat of solidification, evaporation, and sublimation; the sensible, convection, and conduction heats; and the adiabatic and kinetic heating.

Analytical Roughness Model

The analytical model presented here follows the observations and conclusions made by Shin.[3] For rime ice grown at cold temperatures, when heat transfer is high, the impinging water droplets freeze on impact and form beads. For glaze ice formed at warmer temperatures, the ice surface is composed of a smooth zone near the stagnation point and beads formed at the transition between the smooth and rough surfaces. To represent all alternatives, three analytical formulations are developed, assuming that the liquid water mass on a surface can be in a film, rivulet, or bead state. A film is typical of a smooth zone, whereas beads represent a rough zone when droplets are impinging on the surface, and rivulets are typical of a rough zone, where there are no droplets impinging on the surface (Fig. 1). Each model is characterized by a roughness height.

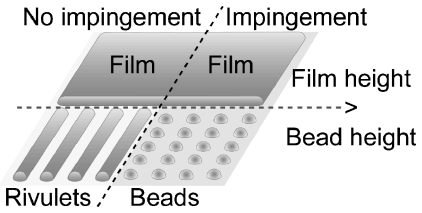

Fig. 1 Water state on the surface.

Film

Film height is calculated by performing a mass balance over the control volume associated with each panel, and when the flow is assumed to be laminar, the film height is

$$e_f = \sqrt{\frac{2}{\tau_w}} \cdot \sqrt{\frac{\mu_w \cdot m_w}{\rho_w \cdot \Delta b \cdot \Delta t}} \cdot C_{\text{cal}} \tag{1}$$

This equation was developed by Al-Khalil et al.[6] and used in thermal de-icing simulations. The calibration parameter C_{cal} is introduced to take into consideration the assumptions made to derive the equation.

The surface water forms a film when its height is greater than the minimum film height, which corresponds to the maximum bead height multiplied by a shape factor. The maximum bead height is the height that the bead can reach before moving. The shape factor is obtained from a mass balance, considering that the water film mass is equal to the summation of all of the bead masses in the control volume. The minimum film height is given by

$$e_{f\min} = \sqrt{\frac{\theta_c - \sin(\theta_c) \cdot \cos(\theta_c)}{2 \cdot \sin(\theta_c)}} \cdot e_b \tag{2}$$

Roughness height is considered to be equal to the wave height[13] and given by

$$\kappa = \tfrac{3}{4} \cdot \tau_w / \mu_w \cdot \sqrt{e_f^3 / g} \tag{3}$$

Rivulets

The water on the surface forms rivulets when the film height is less than the minimum film height, and the control volume is not exposed to impinging droplets. The surface is then wavy and rough. The rivulets are treated as small films of cylindrical form that flow parallel to the wind. The roughness height is equal to the rivulet height, which is assumed to be equal to the bead height before moving:

$$\kappa = e_r \tag{4}$$

Bead

The water on the surface forms beads when the film height is less than the minimum film height and the control volume is in the impingement zone. In the bead model, it is assumed that the impinging droplets form beads on the surface on impact. Under a wet regime (Fig. 2), the beads grow, being partially frozen and partially liquid. This growth ends when the beads reach a maximum height. The growth time is in the order of one second. At this moment, the liquid part runs due to the aerodynamic force, a fraction of which remains trapped in the gaps between the frozen parts of the beads, while the rest flows and becomes runback water.

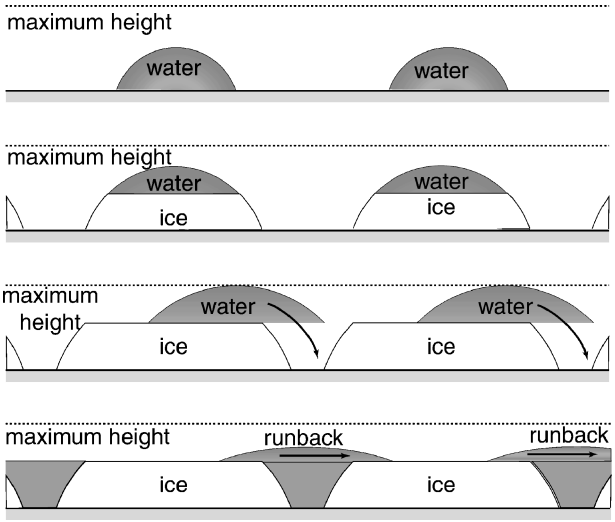

Fig. 2 Bead model in wet regime.

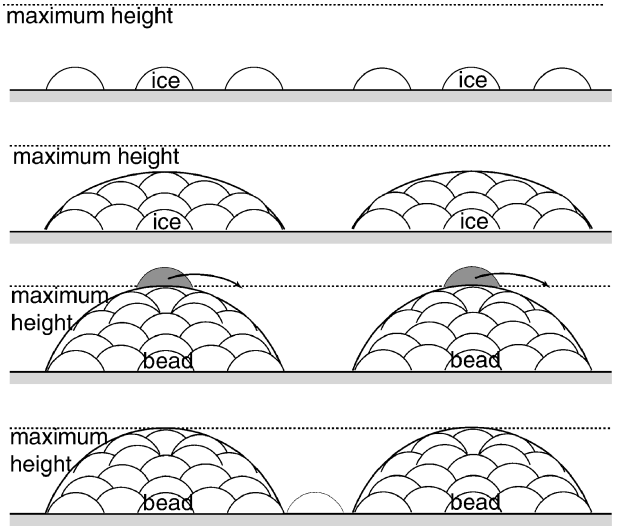

Fig. 3 Bead model in dry regime.

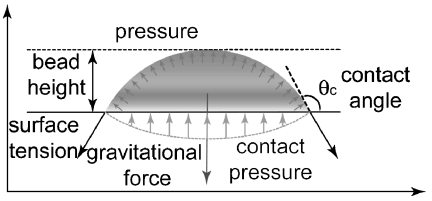

Fig. 4 Forces on a bead.

Under a dry regime (Fig. 3), the droplets solidify entirely upon impact and the solidification time is in the order of a millisecond.

New impinging droplets impact near other droplets to form growing beads. Growth ends when a maximum height is reached. At this time, the new droplets fall, under the aerodynamic force, between two solid beads; the solidifying and growing processes restart with a new bead.

Bead height is calculated from an analysis of the bead growth and the forces acting on it. Figure 4 is a two-dimensional view of a bead with a spherical shape characterized by height and contact angle. The forces acting on a bead are surface tension, gravity, and forces due to internal and contact pressures.

When the surface is inclined and/or wind is present (Fig. 5), a disequilibrium is induced in the bead, which is deformed. The bead becomes nonspherical and is characterized by an hysteresis, which is

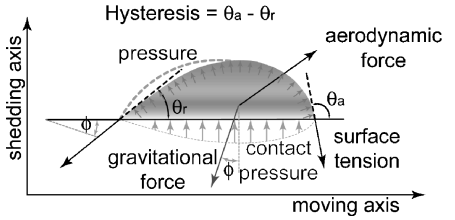

Fig. 5 Forces on a deformed bead.

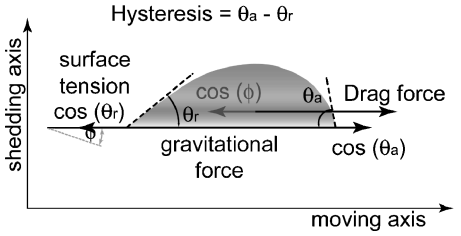

Fig. 6 Forces along the moving axis.

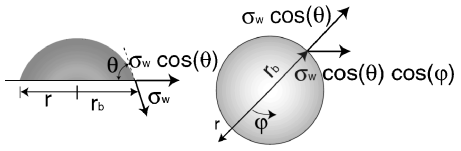

Fig. 7 Rigidity force.

the difference between the maximum and minimum contact angles. The forces acting on the deformed bead are the same as in the preceding case, to which aerodynamic forces drag and lift are added.

It is assumed that a bead moves only under the drag force and that there is not enough lift force to shed the bead. Bead height is a function only of the forces exerted along the moving axis. When it is assumed that the force due to internal pressure is negligible, the forces along the moving axis are the gravitational force component parallel to the surface; the rigidity force, which is the component of the surface tension along the moving axis; and the drag force, which is the aerodynamic force (Fig. 6). The rigidity force is in the direction opposite to the deformation.

To evaluate each force, many assumptions are needed to simplify the calculation. The gravitational force is equal to water density multiplied by bead volume and gravitational acceleration:

$$F_{\text{grav}} = \rho_w \cdot V_b \cdot g \tag{5}$$

Bead volume, calculated for a nondeformed bead, is expressed in terms of bead height and contact angle. The component of the gravitational force parallel to the surface for a nondeformed bead is

$$F_g = \frac{\pi}{3} \cdot g \cdot \rho_w \frac{2 + \cos(\theta_c)}{1 - \cos(\theta_c)} \cdot e_b^3 \cdot |\sin(\varphi)| \tag{6}$$

The rigidity force, which is the component of the surface tension along the moving axis (Fig. 7), is determined by integration of the surface tension multiplied by the bead radius over the bead perimeter:

$$F_\sigma = \int_0^{2\cdot\pi} \sigma_w \cdot \cos(\theta) \cdot \cos(\varphi) \cdot r_b \cdot \mathrm{d}\varphi \tag{7}$$

Bead radius is expressed in terms of its height and the contact angle for a nondeformed bead. The surface tension is expressed in terms of the contact angle and the hysteresis defined earlier (Fig. 8).

It is known that surface tension varies along the perimeter. It is assumed that this variation has a cosinusoidal form and that the hysteresis is low. With these assumptions, the equation is integrated

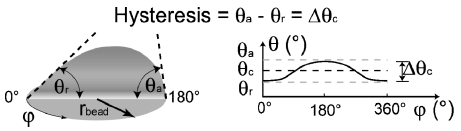

Fig. 8 Hysteresis contact angle distribution.

over the perimeter, considering that the radius varies, as for a nondeformed bead, and is given by

$$F_\sigma = \pi/2 \cdot \sigma_w \cdot [1 + \cos(\theta_c)] \cdot e_b \cdot \Delta\theta_c \tag{8}$$

The drag force is equal to

$$F_D = \tfrac{1}{2} \cdot \rho_a \cdot C_D \cdot A_b \cdot \bar{U}_w^2 \tag{9}$$

where the average wind velocity is calculated at the top of the bead.

The drag coefficient is assumed to be constant at 0.44. This value corresponds to a sphere drag coefficient[14] with a Reynolds number between 1×10^3 and 8×10^5. The frontal cross section is calculated for a nondeformed bead and is expressed in terms of bead height and contact angle. Wind velocity is calculated for a fully turbulent flow and the strain rate, according to the mixing length hypothesis, as follows:

$$F_W = \tau_w \cdot C_G(e_b) \cdot \frac{\theta_c - \sin(\theta_c) \cdot \cos(\theta_c)}{[1 - \cos(\theta_c)]^2} \cdot e_b^2 \tag{10}$$

where the wall shear stress is

$$\tau_w = \tfrac{1}{2} \cdot \rho_a \cdot C_f \cdot U_e^2 \tag{11}$$

The flow coefficient C_G is the nonlinear part of the aerodynamic flow ratio divided by a calibration parameter C_{cal},

$$C_G(e_b) = 1.725/C_{\text{cal}} \cdot [\ln(\tau_w/\mu_a \cdot e_b) + 1.4]^2 \tag{12}$$

The calibration parameter is introduced to take into account the assumptions made to develop the force equation regarding the radius, frontal cross section, and volume of a spherical bead; the drag coefficient of the bead, which is assumed to be a constant value; and the contact angle and hysteresis, which are measured for an ice surface without considering roughness.

Bead height is calculated from the following force balance along the moving axis:

$$\pm F_g \pm F_W - F_\sigma = 0 \tag{13}$$

When the maximum hysteresis is reached, the equilibrium between the aerodynamic, gravitational, and rigidity forces is broken, and the bead begins to move. The maximum height that a bead can reach before moving is determined using the earlier force equation for the maximum hysteresis condition. The contact angle and hysteresis have been measured by Hansman and Turnock[4] on an ice surface, as a function of temperature.

When the aerodynamic and gravitational forces are in the same direction, the roughness height is

$$e_b = \frac{-R_W + \sqrt{R_W^2 + 4 \cdot R_g \cdot \Delta\theta_c}}{2 \cdot R_g} \tag{14}$$

The gravitational flow ratio R_g is the projection of the gravitational force parallel to the surface divided by the rigidity force:

$$R_g = \frac{2}{3} \cdot g \cdot \frac{\rho_w}{\sigma_w} \cdot \left[\frac{2 + \cos(\theta_c)}{\sin^2(\theta_c)}\right] \cdot |\sin(\varphi)| \tag{15}$$

The aerodynamic flow ratio R_w is the projection of the aerodynamic force parallel to the surface divided by the rigidity force:

$$R_W = \frac{2}{\pi} \cdot C_G(e_b) \cdot \frac{\tau_w}{\sigma_w} \cdot \frac{\theta_c - \sin(\theta_c) \cdot \cos(\theta_c)}{\sin^2(\theta_c) \cdot [1 - \cos(\theta_c)]} \tag{16}$$

Roughness height is equal to the height that the bead reaches before moving:

$$\kappa = e_b \tag{17}$$

Remaining Water Mass

The remaining water is the liquid water entrapped in the control volume, and this mass is calculated using a mass balance based on water state (film, rivulets, or beads) and maximum bead height. In a dry regime, this remaining water mass is zero.

For the film mass balance, it is assumed that the remaining water has a minimum film height as follows:

$$m_{\text{rmw}} = \rho_w \cdot A_p \cdot e_{f\,\min} \tag{18}$$

For the rivulet mass balance, it is assumed that the remaining water mass is equal to the unfrozen rivulet, which is computed as the unfrozen film part:

$$m_{\text{rmw}} = \rho_w \cdot A_p \cdot e_f \cdot (1 - f) \tag{19}$$

The remaining water mass for the bead state is related to the admissible liquid water mass when the bead is fully grown. This admissible water mass corresponds to the quantity of water trapped in the volume between frozen bead parts. This mass is the same for all beads uniformly spread over the surface:

$$m_{\text{wadm}} = \rho_w \cdot (1 - f_{bw}) \cdot A_p \cdot e_b \tag{20}$$

Here, the bead liquid fraction f_{bw} is determined when the bead is fully grown. It is the height ratio between the liquid part and the bead, to which is added the volume ratio between the bead and the frozen parts, and given by

$$f_{bw} = \sqrt{\frac{\rho_b}{\rho_w} \cdot \frac{1 - f}{3} \cdot [2 + \cos(\theta_c)]} + f \cdot \frac{\rho_b}{\rho_i} \cdot \frac{f_w}{3} \cdot \frac{2 + \cos(\theta_c)}{1 + \cos(\theta_c)} \tag{21}$$

Bead density is expressed in terms of the liquid and solid bead parts as follows:

$$\rho_b = \rho_i \cdot f + \rho_w \cdot (1 - f) \tag{22}$$

Ice density used in the calculation was determined by Laforte and Allaire[15] for a rotating cylinder. This empirical equation is independent of the cylinder diameter and is valid when the surface temperature is lower than the solidification temperature:

$$\rho_i = 917 \cdot \left(\frac{d_d \cdot U_\infty}{d_d \cdot U_\infty + 2.6 \times 10^{-6} \cdot [T_f - T_s]}\right)^2 \tag{23}$$

As already stated, the admissible liquid water mass is determined using the volumes of the spaces between the frozen bead parts (Fig. 2). When the liquid water does not completely fill the volume between beads, the remaining water mass is equal to the liquid water mass. When the liquid water fills the volume between the frozen bead parts completely, the remaining water mass is equal to the admissible liquid water mass:

$$m_{\text{rmw}} = \begin{cases} m_{\text{wadm}} & \text{if} \quad m_w > m_{\text{wadm}} \\ m_w & \text{if} \quad m_w \le m_{\text{wadm}} \end{cases} \tag{24}$$

The liquid water mass is the part of the incoming water mass on the control volume that remains liquid. It is the summation of the impingement water mass, the incoming runback water mass, and the residual mass, minus the evaporative mass:

$$m_w = (m_{\text{cap}} + m_{\text{rbin}} + m_{\text{resw}} - m_{\text{evap}}) \cdot (1 - f) \tag{25}$$

The residual water mass is equal to the remaining water mass at the preceding time step.

Runback Water Mass

The outgoing runback water mass is equal to the difference between the liquid water mass and the remaining water mass:

$$m_{\text{rbout}} = m_w - m_{\text{rmw}} \tag{26}$$

The incoming runback water mass is equal to the outgoing runback water mass of the preceding control volume.

Shedding Water Mass

It is assumed that liquid water behaves differently on the lower and upper surfaces. It was observed in numerical simulations that the upper surface is best described using a model with runback, whereas the lower surface is best described using a model without runback. Accordingly, a runback model is used on the upper and lower surfaces, but it is assumed that the runback water mass on the lower surface is shed by the aerodynamic force instead of moving to the next control volume. Therefore, the shedding water mass is zero on the upper surface, whereas the runback water mass is zero on the lower surface:

$$m_{\text{shw}} = \begin{cases} m_{\text{rbout}} & \text{on the lower surface} \\ 0 & \text{on the upper surface} \end{cases} \tag{27}$$

Geometric Accretion Model

In general, ice shape is difficult to model when the growth direction is unknown. Therefore, the bisection method was developed to eliminate the iterative process actually employed, which requires small panels and produces a smooth ice-covered surface. The use of the panel bisection method allows for ice to grow continuously in the normal direction to the surface of the object, which is the natural growth direction. To achieve this growth, the ice sections are limited by the bisection of angles with adjacent neighboring panels. The use of the panel bisection method is shown in Fig. 9. Each bisection is characterized by a slope *mb* and the *x* and *y* coordinates of the origin node:

$$y - y_i = mb_i \cdot (x - x_i) \tag{28}$$

The new panels are calculated using previous nodes coordinates (1, 2, and $n1$), the bisection equation at node 2 and accreted ice surface (Fig. 9). The accreted ice on the panel is equal to the quadrilateral delimited by the bisection crossing nodes 1 and 2.

If the positions of nodes 1, 2, and $n1$ are known, then the node n_2 coordinates are given by

$$xn_2 = x_2 - \frac{(y_2 - yn_1) \cdot (x_2 - x_1) - (x_2 - xn_1) \cdot (y_2 - y_1) + 2 \cdot A_i}{(y_2 - yn_1) - mb_2 \cdot (x_2 - xn_1)} \tag{29}$$

$$yn_2 = y_2 - mb_2 \cdot \frac{(y_2 - yn_1) \cdot (x_2 - x_1) - (x_2 - xn_1) \cdot (y_2 - y_1) + 2 \cdot A_i}{(y_2 - yn_1) - mb_2 \cdot (x_2 - xn_1)} \tag{30}$$

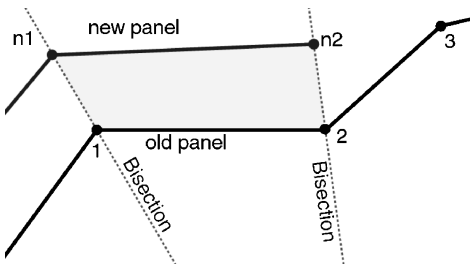

Fig. 9 Building of new panel.

Table 1 Meteorological conditions

Condition	Value
Accretion time	360 s
Angle of attack	4 deg
Chord	0.5334 m
Air speed	67.05 m/s
Atmospheric pressure	101,300 Pa
Liquid water content	1 g/m^3
Median volumetric diameter	20 μm

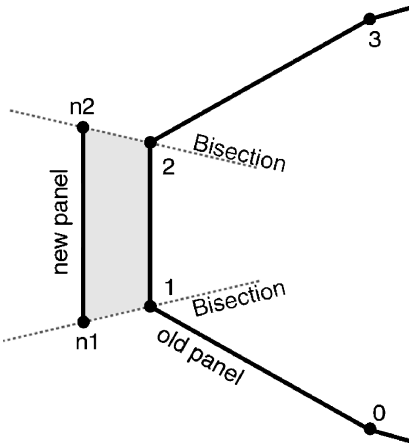

Fig. 10 Stagnation point.

The new panels are built starting from the stagnation point, where the runback water mass is zero, going toward the lower and upper surfaces (Fig. 10).

The method requires an additional equation at the stagnation point to close the system. This equation was developed by assuming that the new panel is parallel to the old one:

$$\frac{y_2 - y_1}{x_2 - x_1} = \frac{yn_2 - yn_1}{xn_2 - xn_1} \tag{31}$$

Results

Case Studies

The two-dimensional CIRAMIL code is the combination of the two-dimensional CIRA code, which calculates the airflow and trajectories, and the AMIL code, which calculates the convective heat transfer coefficient, roughness height, heat and mass balances, and ice addition. This code was evaluated by performing numerical simulations on a NACA0012 wing profile under the geometric, aerodynamic, and meteorological conditions shown in Table 1. The computation was performed at seven temperatures (−28.3, −19.4, −13.3, −10.0, −7.8, −6.1, and −4.4°C) in both dry and wet regimes.

The two-dimensional CIRAMIL predicted ice shapes are compared to those obtained experimentally under the same conditions in the NASA John H. Glenn Research Center at Lewis Field Icing Research Tunnel (IRT) and predicted using the two-dimensional LEWICE/IBL code and shown by Shin and Bond.[1] They are also compared to the ice shapes predicted using the two-dimensional CIRA code shown in the CIRA user manual.[7] Repeatability of the Shin and Bond[1] experimental ice shapes is for two runs, but no standard code error is given. The comparison between predicted and measured ice shapes can only be qualitative, as in most papers on the subject. In the IRT wind tunnel, the wing was vertical, meaning that gravitational acceleration was perpendicular to the wind. For the model, bead height is calculated for a flying configuration where the gravity acceleration component and wind are in the same direction. However, this equation can be used for the IRT wind tunnel when the gravitational force is small compared to the drag force. For this comparison, the predicted and measured ice shapes are those presented after 6 min of accretion. The liquid water mass and the roughness height distribution are presented for the final time step

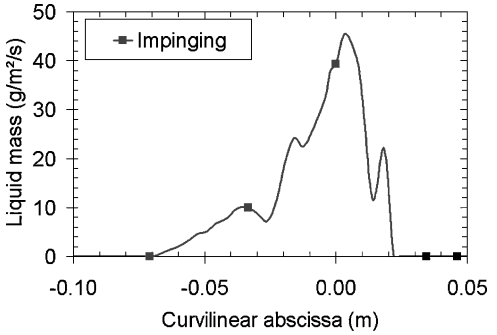

Fig. 11 Liquid water mass at −28.3°C.

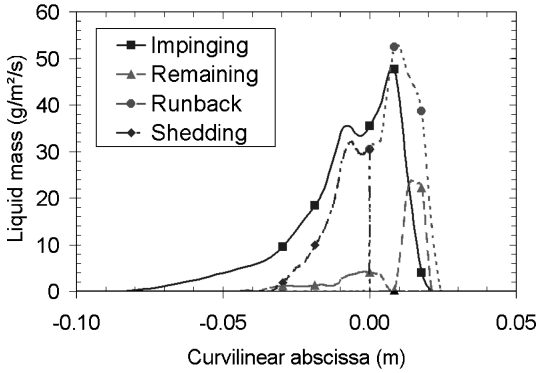

Fig. 12 Liquid water mass at −4.4°C.

as a function of the curvilinear abscissa. The curvilinear abscissa follows the airfoil surface starting at the stagnation point. It has positive values for the upper surface and negative ones for the lower surface.

Liquid Water Mass

Figures 11 and 12 show the liquid water mass distribution in the control volume calculated for the final time step at −28.3 and −4.4°C. In the dry regime at −28.3°C (Fig. 11), the input liquid water mass comes from the impinging droplets only.

In the wet regime at −4.4°C (Fig. 12) on the upper surface, the input liquid water mass comes from the impinging droplets, as well as the remaining and runback water masses.

On the lower surface, the input liquid water mass is composed of impinging droplets and remaining water, because the runback water is assumed to be shed by aerodynamic force.

Roughness Height

Figure 13 shows the roughness height distribution calculated at −4.4 and −28.3°C for the final time step. Under the dry regime at −28.3°C, supercooled water droplets freeze on impact and form beads on the surface.

The roughness height is at a maximum at the stagnation point and decreases toward the ice end. Under the wet regimes at −4.4°C, the liquid water on the upper surface flows to the next control volume as a film, and the roughness is the wave height. For this flow state, the roughness height is at a minimum at the stagnation point, this value increases rapidly to reach a maximum, after which it decreases toward the ice end. For the lower surface, near the stagnation point the liquid water, before shedding, is as a film. For this flow state, roughness height is at a minimum at the stagnation point, and increases gradually to reach a maximum value, after which it decreases toward the ice end.

The roughness results are summarized in Table 2. Under the dry regime, the maximum roughness height is greater on the lower surface than on the upper surface and is independent of temperature. Under the wet regime, the maximum roughness height is greater on the upper than on the lower surface. On the upper surface, this height increases and reaches a maximum, after which it decreases.

Table 2 Roughness height in millimeters at final time

		Upper		Lower	
Temperature, °C	Regime	Maximum	Average	Maximum	Average
−28.3	Dry	—	0.23	—	0.48
−19.4	Dry	—	0.21	—	0.44
−13.3	Wet	3.34	0.09	1.20	0.40
−10.0	Wet	3.70	0.05	1.95	0.24
−7.8	Wet	5.62	0.03	1.41	0.19
−6.1	Wet	4.95	0.04	1.19	0.14
−4.4	Wet	4.65	0.02	1.27	0.13

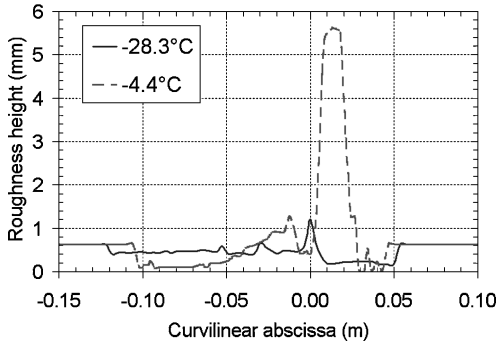

Fig. 13 Roughness distribution.

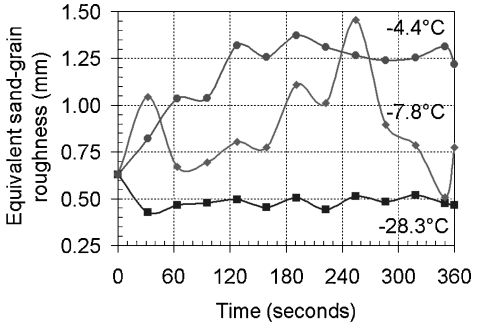

Fig. 14 Equivalent sand-grain roughness.

On the lower surface, this height decreases and reaches a minimum, after which it increases. On the upper surface, the average roughness height is independent of the temperature and is very small, whereas on the lower surface, it decreases with increasing temperature.

Figure 14 shows the time dependence of the roughness distribution expressed in terms of equivalent sand-grain roughness, which was calculated using

$$\kappa_s = \frac{\int_{-s_{\text{lower}}}^{s_{\text{upper}}} \kappa \cdot \mathrm{d}s}{\int_{-s_{\text{lower}}}^{s_{\text{upper}}} \mathrm{d}s} \tag{32}$$

Figure 14 shows that, in the dry regime at −28.3°C, the equivalent sand-grain roughness oscillates slightly around an average value of 0.5 mm. In the wet regime at −4.4°C, this roughness increases from 0.63 to 1.3 mm, after which it oscillates around this average value. For the middle case at −7.8°C, the equivalent sand-grain roughness increases to reach a maximum value of 1.5 mm and then decreases to a value of about 0.7 mm after 6 min of accretion, thus indicating that this roughness is not stabilized. The experimental observations made by Shin[3] include: that roughness does not vary with time for rime, increases as a function of time for glaze, and increases with increasing temperature.

Figure 15 shows a comparison of the computed average equivalent sand-grain roughness over the time period with those calculated with the empirical Shin and Bond[1] correlation:

$$\kappa_s = \kappa_0 \times (0.6839) \times (0.047 \cdot T_0 - 11.27) \times (0.571 + 0.246 \cdot \mathrm{LWC} + 1.257 \cdot \mathrm{LWC}^2) \tag{33}$$

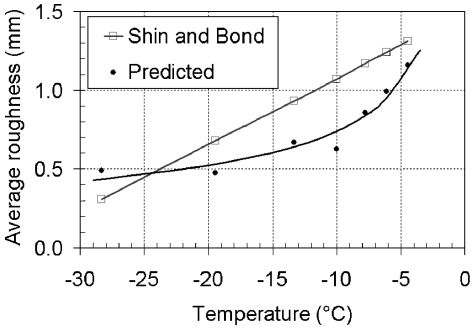

Fig. 15 Average equivalent sand-grain roughness.

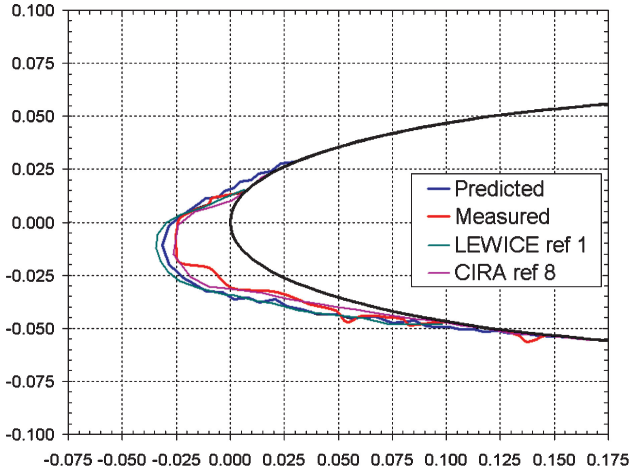

Fig. 16 Ice shape at −28.3°C.

where liquid water content (LWC) is in grams per cubic meter. This correlation was determined by selecting the equivalent sand-grain roughness that gives the best fit between the experimental ice shapes and those computed using the two-dimensional LEWICE/IBL. The equivalent sand-grain roughness of the airfoil surface, κ_0, used in the correlation is 0.628 mm.

The equivalent sand-grain roughness values calculated from local roughness height are of the same order of magnitude as those calculated with the Shin and Bond[1] correlation and increase as temperature increases. However, the empirical equivalent sand-grain roughness increases linearly with temperature, whereas that calculated using the two-dimensional CIRAMIL code increases according to a power law inversely proportional to the degree of supercooling. The following power law was found to fit better than exponential or logarithmic functions:

$$\kappa_s = 2.82 \cdot (T_f - T)^{-0.6} \tag{34}$$

Ice Accretion Shapes

Figures 16–22 show the ice shapes predicted after 6 min of simulation using the two-dimensional CIRAMIL, two-dimensional LEWICE/IBL,[1] and two-dimensional CIRA[7] codes, the former being compared to those measured experimentally by Shin and Bond.[1] For the −28.3°C (Fig. 16) and −19.4°C (Fig. 17) cases, ice shapes are typical of a dry regime where only rime ice occurs. Predicted and measured ice shapes are essentially the same, except for the predicted volume, which is slightly greater than that measured. No significant difference can be observed between the two-dimensional CIRAMIL, two-dimensional LEWICE/IBL, and two-dimensional CIRA codes, except that for the two-dimensional LEWICE/IBL code the volume is slightly greater than that of measured shapes. For the other cases (−13.3°C, Fig. 18; −10.0°C, Fig. 19; −7.8°C, Fig. 20; −6.1°C, Fig. 21; and −4.4°C, Fig. 22), the predicted ice shapes are characteristic of the wet regime, where a horn forms on the upper surface with a small hollow at the stagnation point. Both predicted and measured ice shapes look similar, but the predicted

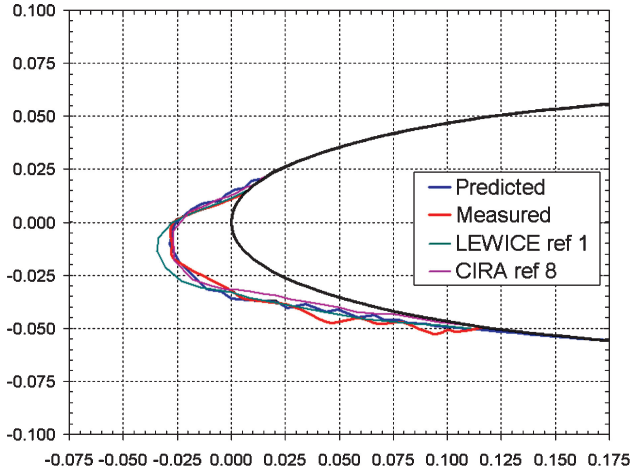

Fig. 17 Ice shape at −19.4°C.

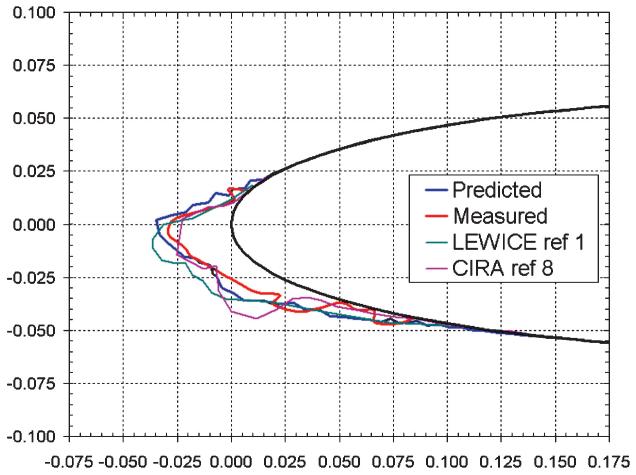

Fig. 18 Ice shape at −13.3°C.

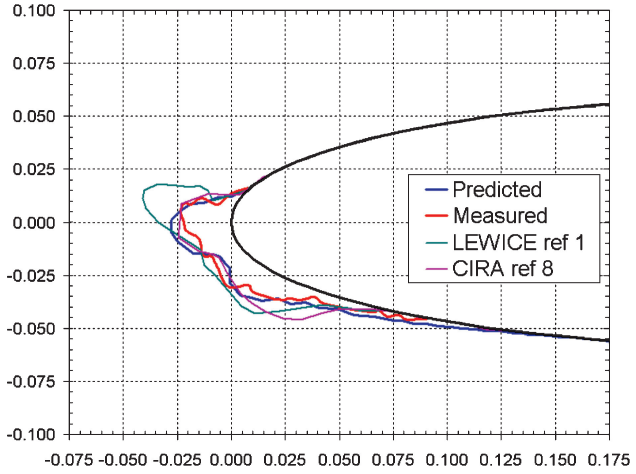

Fig. 19 Ice shape at −10.0°C.

volume is slightly greater than the one measured. For temperatures lower than or equal to −7.8°C, the two-dimensional CIRAMIL predicted ice shapes are closer to those measured than for the two-dimensional LEWICE/IBL and two-dimensional CIRA codes. For temperatures above −7.8°C, the two-dimensional CIRAMIL code cannot produce the horn on the upper surface, as well as the two-dimensional LEWICE/IBL and two-dimensional CIRA codes.

In most cases, the ice profiles are jagged along the wing in the region where the ice ends, because the ice mass shows a nonuniform

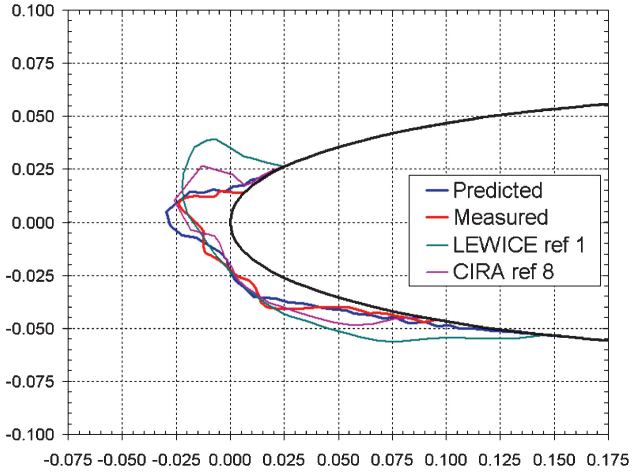

Fig. 20 Ice shape at −7.8°C.

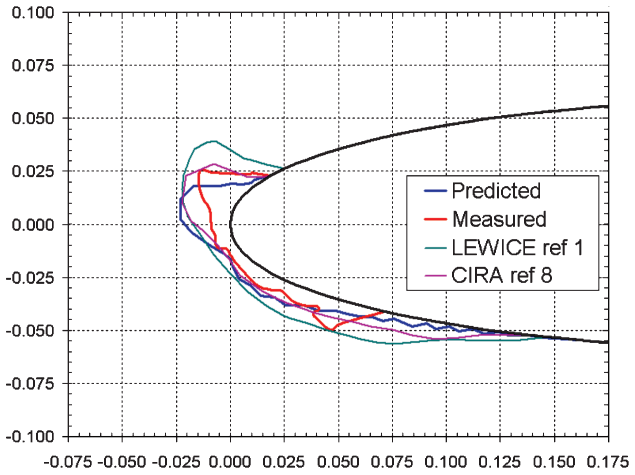

Fig. 21 Ice shape at −6.1°C.

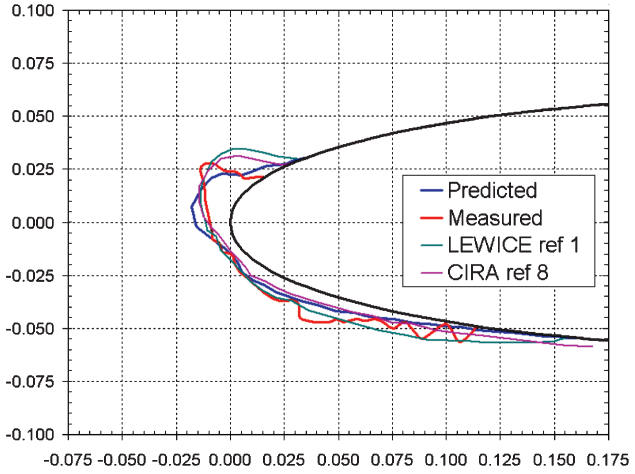

Fig. 22 Ice shape at −4.4°C.

growth. In three cases at temperatures above −7.8°C, the predicted and measured points where the ice ends are not located at the same position. For temperature at −4.4°C, the predicted and measured ice shapes are similar on the lower surface, but different on the upper surface because the horn is not formed in the same place. This is probably because the local roughness is too low, resulting in too small a local convective heat transfer coefficient. At −7.8°C, the predicted and measured ice shapes are similar. This case was chosen to calibrate the roughness model because it corresponds to accretion

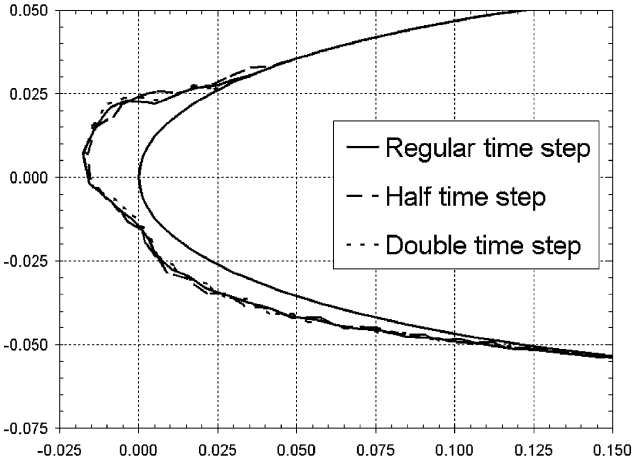

Fig. 23 Time step effect at −4.4°C.

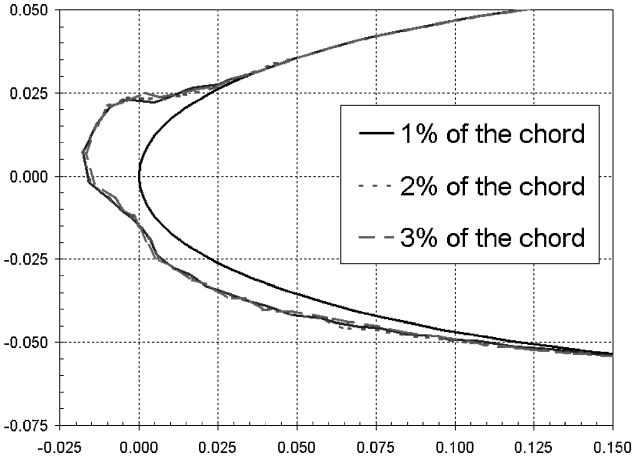

Fig. 24 Panel length effect at −4.4°C.

in a half-dry and half-wet regime. The calibration was performed by adjusting parameter C_{cal} to a value of 15, where the better ice shape fit is obtained.

Time Step Effect

Figure 23 shows the final ice shape predicted at −4.4°C with the two-dimensional CIRAMIL code for three different time steps, 15.9, 31.8, and 63.6 s, the middle value being the one used earlier. Figure 23 shows that ice shape is not affected by reducing or increasing the regular time step by a factor of two. The independence of results with such time step variations shows that the time step used for the initial computation is sufficiently small to obtain accurate results.

Panel Length Effect

Figure 24 shows the influence of panel length on the final ice shape predicted at −4.4°C. Figure 24 shows that increasing the panel length by a factor of two or three does not affect ice shape, which shows that the panel length used to define the airfoil is adequate to obtain accurate results.

Analysis

Thermodynamic Model

The model used can predict ice shapes on the leading edge of an airfoil, which are comparable to those obtained experimentally, and in some cases, they fit better than those obtained with the available models. The predicted ice shapes are similar to those measured, with similarity increasing as temperature decreases. The maximum value of the convective heat transfer coefficient is found on the upper surface, where the horn forms. As observed experimentally,

the length of the wet zone near the stagnation point increases with temperature.

Roughness Models

The physical formulations developed in dry and wet regimes to calculate the local roughness height produce an average equivalent sand-grain roughness in the same order of magnitude as that calculated in Shin and Bond's empirical correlation.[1] However, local roughness obtained by simulation is very different. This difference can favor formation of horn and surface asperities where roughness and local convective heat transfer coefficients are higher. Interdependence between the roughness and friction coefficient does not lead to numerical instability, but, rather, to oscillations around an average value. It has been shown that the analytical model used to calculate the roughness is independent of panel length and time step.

Mass Models

The model proposed to calculate the remaining, runback, and shedding water masses yields a good representation of ice shapes measured in a wind tunnel. The free water flows as a film, beads, or rivulets on the upper surface and is shed on the lower surface. A small water mass resides on the surface, depending on the intensity and direction of aerodynamic and gravitational forces. The runback water mass on the upper surface and the shedding water mass on the lower surface increase with temperature, as well as the remaining water mass. The ice accretion mass and volume decrease as temperature increases, whereas its density increases with temperature.

Bisection Method

According to the numerical simulation results, the proposed geometric accretion model based on the panel bisection method is a good representation of ice shape measured in a wind tunnel. The method can reproduce horn and spikes observed experimentally in a wet regime. The method is independent of panel length and time step. The bisection method is robust enough to work with small or large ice masses on panels without altering the final shape.

Conclusions

Based on the final ice shapes, the analytical model development that includes local roughness height, remaining runback, and shedding water masses, as well as the bisection method, can generate the complex ice shapes with horns observed experimentally with the same accuracy as, or better then, available models. However, in most cases, the predicted icing volume is slightly larger than that measured. The predicted ice shapes obtained by the numerical simulation show that the runback water is dominant on the upper surface, whereas shedding water dominates on the lower surface. The ice shape is strongly dependent on the local roughness, which is directly related to the friction coefficient and, indirectly, to the convective heat transfer coefficient.

Acknowledgments

This work was financed by the Anti-Icing Materials International Laboratory. The authors would like to thank the Italian Aerospace Research Center for providing, the air flow, droplet trajectory, and collection efficiency codes. We also thank Patrick Louchez who started the project.

References

[1]Shin, J., and Bond, T., "Experimental and Computational Ice Shapes and Resulting Drag Increase for a NACA 0012 Airfoil," NASA TM 105743, Jan. 1992.

[2]Nikuradse, J., "Strö In Rauher Rohen, VDI-Forshungsheft 361, 1933; also, Laws of Flow in Rough Pipes," NACA TM 1292, 1950.

[3]Shin, J., Characteristics of Surface Roughness Associated with Leading Edge Ice Accretion," *Jouranl of Aircraft*, Vol. 33, No. 2, 1996, pp. 316–321; also AIAA Paper 94-0799, Jan. 1994.

[4]Hansman, R. J., Jr., and Turnock, S. R., "Investigation of Surface Water Behavior During Glace Ice Accretion," *Journal of Aircraft*, Vol. 26, No. 2, 1989, pp. 140–147; also AIAA Paper 88-0015, 1988.

[5]Al-Khalil, K. M., Keith, T. G., Jr., and De Witt, K. J., "Further Development of an Anti-Icing Runback Model," AIAA Paper 91-0266, Jan. 1991.

[6]Al-Khalil, K. M., Keith, T. G., De Witt, K. J., Jr., Nathman, J. K., and Dietrich, D. A., "Thermal Analysis of Engine Inlet Anti-Icing Systems," *Journal of Propulsion and Power*, Vol. 6, 1990, pp. 628–634; also AIAA Paper 89-0759, 1989.

[7]Mingione, G., and Brandi, V., "Ice Accretion Prediction on Multielements Airfoils," *Journal of Aircraft*, Vol. 35, No. 2, 1998.

[8]Messinger, B. L., "Equilibrium Temperature of an Unheated Icing Surface as a Function of Airspeed," *Journal of the Aeronautical Sciences*, Vol. 20, No. 1, 1953, pp. 29–42.

[9]Wright, W. B., "Update to the NASA Lewis Ice Accretion Code LEWICE," NASA Rept. 195387, May 1994.

[10]Gent, R. W., "TRAJICE2, A Combined Water Droplet and Ice Accretion Prediction Program for Aerofoil," Royal Aerospace Establishment (RAE) Technical Rept. TR90054, Farnborough, Hampshire, Nov. 1990.

[11]Guffond, D., Hedde, T., and Henry, R., "Overview of Icing Research at ONERA," *Advisory Group for Aerospace Research and Development/Fluid Dynamics Panel Joint International Conference on Aircraft Flight Safety—Actual Problems of Aircraft Development*, 31 Aug.–5 Sept. 1993.

[12]Paraschivoiu, I., Overview of J.-A. Bombardier Aeronautical Chair Projects at École Polytechnique de Montréal," *1st Bombardier International Workshop on Aircraft Icing/Boundary-Layer Stability and Transition*, edited by I. Paraschivolu, Ecole Polythecnique, Bombardier Canadair, Montreal, Quebec, Canada, Sept. 1994.

[13]Gerhart, P. M., Gross, R. J., and Hochstein, J. I., *Fundamentals of Fluid Mechanics*, 2nd ed., Addison–Wesley, Reading, MA, 1992, pp. 845–847.

[14]Janna, W. S., *Introduction to Fluid Mechanics*, 2nd ed., PWS Publishing, Boston, 1991, p. 254.

[15]Laforte, J.-L., and Allaire, M. A., "Évaluation du givromètre d'Hydro-Québec à différentes intensités de givrage sec et humide," Hydro-Québec Inst., Études et Normalisation, Équipement de Transport Co, Rept. HQ-92-02, Montréal, Québec, Canada, Jan. 1992.